

Acoustic three-terminal controller with amplitude control for nonlinear seismic metamaterials

Cite as: AIP Advances **12**, 075312 (2022); <https://doi.org/10.1063/5.0099843>

Submitted: 19 May 2022 • Accepted: 23 June 2022 • Published Online: 13 July 2022

Yuanyuan Li, Jiancheng Liu, Zhaoyu Deng, et al.



View Online



Export Citation



CrossMark

ARTICLES YOU MAY BE INTERESTED IN

[Acoustic coding metamaterial based on non-uniform Mie resonators](#)

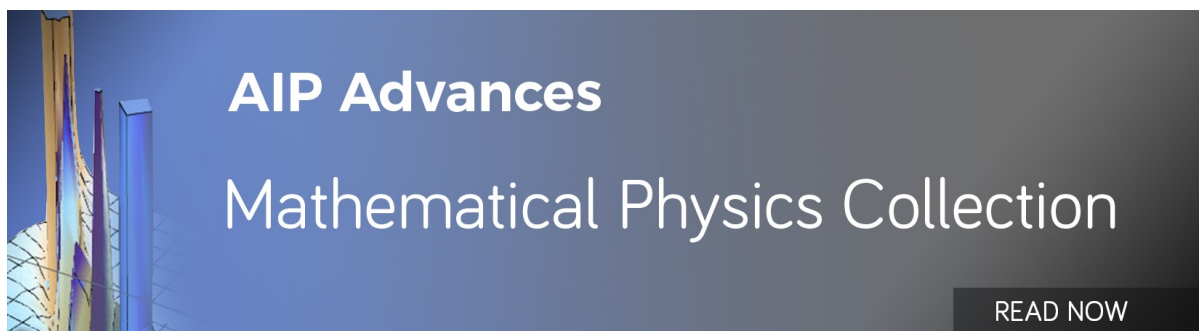
[Applied Physics Letters **120**, 163501 \(2022\); https://doi.org/10.1063/5.0071897](#)

[Effect of interaction of adjacent unit-cells on wave propagation in coupled mass-in-mass metamaterials](#)

[The Journal of the Acoustical Society of America **151**, 4228 \(2022\); https://doi.org/10.1121/10.0011789](#)

[Non-Hermitian skin effect in a phononic beam based on piezoelectric feedback control](#)

[Applied Physics Letters **121**, 022202 \(2022\); https://doi.org/10.1063/5.0097530](#)



AIP Advances
Mathematical Physics Collection

READ NOW

The banner features a blue gradient background with abstract geometric shapes and patterns on the left side. The AIP Advances logo is at the top, and the Mathematical Physics Collection title is in the center. A "READ NOW" button is in the bottom right corner.

Acoustic three-terminal controller with amplitude control for nonlinear seismic metamaterials

Cite as: AIP Advances 12, 075312 (2022); doi: 10.1063/5.0099843

Submitted: 19 May 2022 • Accepted: 23 June 2022 •

Published Online: 13 July 2022



View Online



Export Citation



CrossMark

Yuanyuan Li,¹ Jiancheng Liu,¹ Zhaoyu Deng,¹ Menyang Gong,¹ Kunqi Huang,¹ Yun Lai,^{1,a)} and Xiaozhou Liu^{1,2,b)}

AFFILIATIONS

¹ Key Laboratory of Modern Acoustics, Institute of Acoustics and School of Physics, Collaborative Innovation Center of Advanced Microstructures, Nanjing University, Nanjing 210093, China

² State Key Laboratory of Acoustics, Institute of Acoustics, Chinese Academy of Sciences, Beijing 100190, China

^{a)}E-mail: laiyun@nju.edu.cn

^{b)}Author to whom correspondence should be addressed: xzliu@nju.edu.cn

ABSTRACT

To design and optimize seismic metamaterials, the impacts of nonlinearity in different locations of locally resonant acoustic metamaterials on the dispersions and the variation of amplitude-dependent bandgaps are investigated in this paper. The research used theoretical calculations, namely, Lindstedt-Poincaré perturbation method and prediction method, and combined finite-element simulation. Summarizing from our research, the lower bandgap is sensitive when exposed to amplitude stimulation, when there arise nonlinear characteristics between matrices; while nonlinearity appears within the interior oscillator, amplitudes obtain a more intense influence on the bandgap, introducing an enormous magnitude of deviation between the upper bandgap and the lower bandgap. Based on the peculiar frequency-shift characteristics, an acoustic three-terminal controller is proposed as a conventional subsize acoustical device and nonlinear seismic metamaterials component. This controller enables the realization of modulating the value of output signals by adjusting the quantitative loading on the control port, without changing the input signals and the parameters of the apparatus validated with the finite-element simulation. The work may offer potential applications in low-frequency vibration reduction and external-controllable multi-functional acoustical devices.

© 2022 Author(s). All article content, except where otherwise noted, is licensed under a Creative Commons Attribution (CC BY) license (<http://creativecommons.org/licenses/by/4.0/>). <https://doi.org/10.1063/5.0099843>

I. INTRODUCTION

Over the years, research studies on seismic metamaterials (SMs) have gained more and more significance due to the tremendous menaces of global seismic activities. SM is classified as one of the acoustic metamaterials (AMs). The concepts of AMs originate from the realization of manipulating electromagnetic waves with photonic crystals, which represent materials with functional artificial microstructure. Generally speaking, the form of periodic inclusions is utilized to generate local resonance and instability in the host materials,^{1–5} to achieve unusual manipulation of elastic waves propagation, such as frequency bandgap,^{6–8} enhanced wave-guide capability,^{9,10} and high-energy absorption.^{11–13} There are two disparate ways of constructing AMs bandgap: the Bragg scattering mechanism and the locally resonant mechanism. The former makes use of the superposition of reflected waves between adjacent units,

and the corresponding elastic wavelength of the first bandgap's central frequency is twice the lattice constant. The latter was proposed by Liu in 2000,⁷ and after that extensive research studies have been executed.^{3,6,14–19} AMs, based on the locally resonant mechanism, exhibit dynamic phenomenon of resonance in the host materials, reveal frequency-dependent characteristics, such as effective negative density, negative modulus, and negative refraction, and possess subwavelength acoustic regulation characteristics. As a consequence, locally resonant acoustic metamaterials' (LRAMs) bandgap peculiarity can effectively inhibit the propagation of low-frequency elastic waves. Seismic waves' frequency is normally located between 0.10 and 20.00 Hz. LRAMs lay the foundation of SMs and enjoy great application prospects in mechanical damping and building protection.

Locally resonant seismic metamaterial (LRSMS) is realized with arrangements of a series of artificial^{20–25} or natural^{26,27} resonators.

On this basis, bandgaps introduced by resonance are used to attenuate or transform seismic wave energy, to avoid destruction caused by seismic wave energy. However, LRAMs, at present, occupy too much space to change their parameters without a hitch once they have been well set. It is inconvenient for us to adjust its bandgap range to suit complex practical applications. With the development of investigations, nonlinear acoustic metamaterials (NLAMs) have caught more and more attention. Nonlinearity causes amplitude's impact on the structure, which attracts plenty of research on its dynamic response characteristics.^{28–31} Scholars have established mathematical analysis methods, such as the perturbation method, multiple time scales method, and harmonic balance method.^{32–35} Focusing on nonlinear locally resonant acoustic metamaterials (NLRAMs), Zhou³⁶ analyzed the propagation of wave packets in weak-NLRAMs with nonlinearity existing in the matrix and explained the mechanism of the structure's nonlinear wave through spectral analysis. Zivieri *et al.*³⁷ based on nonharmonic mass-spring and mass-in-mass periodic chain solutions' spatiotemporal decomposition hypothesis, compared the nonlinear dispersion relations of two systems under different amplitudes with theoretical derivation and finite-element simulation. Kulkarni and Manimala³⁸ accomplished passive bias propagation stimulated by elastic longitudinal wave and provided evidence for passive bias phenomenon with contact hardening response test. Fiore *et al.*³⁹ raised an attenuating mechanism to design specific LRAMs to fulfill low-frequency wide range sound energy attenuation with few nonlinear units.

On the contrary, the contrast investigation of loading nonlinear parameters on separate positions in matrix and oscillator and the quantitative relationships between amplitude and bandgap are neglected in those above investigations.^{36–39} As a consequence, the object of study selects the mass-in-mass model in LRAMs and investigates a linear structure and two kinds of cubic softening nonlinear structures: the external matrix and the internal oscillator are linearly connected (EIL), only the spring between two external matrices is nonlinear (EEN), and only the spring between the internal oscillator and the external matrix is nonlinear (IEN) to make contrast research. A prediction method is proposed to acquire approximate solutions of dispersion relations, and the feasibility of this method is validated by comparison with the Lindstedt–Poincaré (L–P) perturbation method. The influence of internal parameters and external amplitude stimulations on the forbidden band of EEN and IEN is analyzed. Furthermore, transmission factor curves of three structures under different stimulations are obtained through finite-element simulation, analyzing the dynamic response of EEN and IEN under different amplitudes with single-frequency and dual-frequency stimulations. The quantitative relationships between external stimulations and bandgap shifts are studied. On this basis, the invention related to a new acoustic device, the acoustic three-terminal controller (ATC), is proposed to optimize the original SMs.

II. THEORETICAL ANALYSIS OF NONLINEAR PERIODIC CHAINS

A. L–P perturbation method and prediction method

As shown in Fig. 1, unidimensional periodic NLAMs originate from a locally resonant mechanism. Each unit consists of an

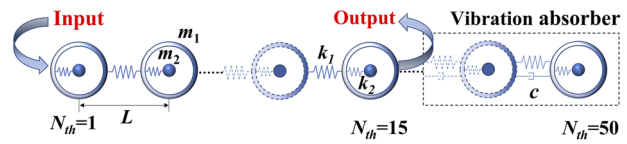


FIG. 1. Schematic of LRAM.

external matrix mass, m_1 , an interior oscillator mass, m_2 , a spring used to connect units having stiffness, k_1 , and a spring between m_1 and m_2 having stiffness, k_2 , and the distance between each unit is L . Inherent frequency $\omega_d = \sqrt{k_2/m_2}$, and u_n and v_n represent the displacement of the external matrix and the interior oscillator attachment when $N_{th} = n$. N_{th} stands for the unit ordinal. Using the introducing nonlinear stiffness parameter, Γ , and perturbation parameter, ε , two different sorts of occasions in which k_1 and k_2 are nonlinear, respectively, are considered so that the restoring force can be expressed as $F_1^{nl} = k_1 u + \varepsilon \Gamma_1 u^3$ and $F_2^{nl} = k_2 u + \varepsilon \Gamma_2 u^3$ individually, and the L–P perturbation method is used to carry out the research.

When $N_{th} = n$, the kinematic equations of the interior oscillator and the external matrix in the IEN structure are as follows:

$$\begin{cases} m_1 \ddot{u}_n + k_1(2u_n - u_{n-1} - u_{n+1}) + k_2(u_n - v_n) + \varepsilon \Gamma_2 (u_n - v_n)^3 = 0, \\ m_2 \ddot{v}_n + k_2(v_n - u_n) + \varepsilon \Gamma_2 (v_n - u_n)^3 = 0. \end{cases} \quad (1)$$

After that, the parameters of the external mass and the interior oscillator are normalized $\bar{m}_1 = \frac{m_2}{m_1}$, $\bar{k}_1 = \frac{k_2}{k_1}$, and $\bar{\Gamma}_2 = \frac{\Gamma_2}{k_2}$. It can be obtained from Eq. (1) that

$$\begin{cases} \bar{k}_1 \Omega^2 \frac{\partial^2 u_n}{\partial \tau^2} + (2u_n - u_{n-1} - u_{n+1}) + \bar{k}_1(u_n - v_n) + \bar{k}_1 \varepsilon \bar{\Gamma}_2 (u_n - v_n)^3 = 0, \\ \Omega^2 \frac{\partial^2 v_n}{\partial \tau^2} + (v_n - u_n) + \varepsilon \bar{\Gamma}_2 (v_n - u_n)^3 = 0, \end{cases} \quad (2)$$

where $\Omega = \omega/\omega_d$ represents dimensionless frequency and $\tau = \omega t$ acts as dimensionless time. Introducing the first-order correction, the perturbation expansion is executed, aiming at dimensionless frequency, the displacement of matrix, and the displacement of oscillator,

$$\begin{aligned} \Omega &= \Omega_0 + \varepsilon \Omega_1 + O(\varepsilon^2), \quad u_n = u_n^{(0)} + \varepsilon u_n^{(1)} + O(\varepsilon^2), \\ v_n &= v_n^{(0)} + \varepsilon v_n^{(1)} + O(\varepsilon^2). \end{aligned} \quad (3)$$

On this basis, the first-order correction is substituted into Eq. (2), and the zero-order and first-order factors ε^0 and ε^1 of the oscillator's kinematic equations are separated,

$$\varepsilon_0 \begin{cases} \frac{1}{m_1} \Omega_0^2 \frac{\partial^2 u_n^{(0)}}{\partial \tau^2} + \frac{1}{k_1} (2u_n^{(0)} - u_{n-1}^{(0)} - u_{n+1}^{(0)}) + (u_n^{(0)} - v_n^{(0)}) = 0, \\ \Omega_0^2 \frac{\partial^2 v_n^{(0)}}{\partial \tau^2} + (v_n^{(0)} - u_n^{(0)}) = 0, \end{cases} \quad (4.1)$$

$$(4.2)$$

$$\varepsilon_1 \begin{cases} \frac{1}{m_1} \Omega_0^2 \frac{\partial^2 u_n^{(1)}}{\partial \tau^2} + \frac{2\Omega_0\Omega_1}{m_1} \frac{\partial^2 u_n^{(0)}}{\partial \tau^2} + \frac{1}{k_1} (2u_n^{(1)} - u_{n-1}^{(1)} - u_{n+1}^{(1)}) + (u_n^{(1)} - v_n^{(1)}) + \bar{\Gamma}_2 (u_n^{(0)} - v_n^{(0)})^3 = 0, \\ \Omega_0^2 \frac{\partial^2 v_n^{(1)}}{\partial \tau^2} + 2\Omega_0\Omega_1 \frac{\partial^2 v_n^{(0)}}{\partial \tau^2} + (v_n^{(1)} - u_n^{(1)}) + \bar{\Gamma}_2 (v_n^{(0)} - u_n^{(0)})^3 = 0, \end{cases} \quad (5.1)$$

$$(5.2)$$

The harmonic solution of this system is assumed as $u_n^{(0)} = \frac{A_0}{2} e^{inqL} e^{i\tau} + \frac{A_0^*}{2} e^{-inqL} e^{-i\tau}$ and $v_n^{(0)} = \frac{B_0}{2} e^{inqL} e^{i\tau} + \frac{B_0^*}{2} e^{-inqL} e^{-i\tau}$, where q is the wave number, A_0, A_0^* stand for the sound-wave amplitude of the external matrix and its conjugate, and B_0, B_0^* are the sound-wave amplitude of the interior oscillator and its conjugate. In the following study, the complex conjugate is expressed by $c \cdot c \cdot \kappa = qL$, $\eta_w = \frac{1}{1-\Omega_0^2}$, and the zero-order and first-order governing equations are obtained,

$$(1 - \Omega_0^2) [-\bar{k}_1 \Omega_0^2 + 2\bar{m}_1 (1 - \cos \kappa)] - \bar{k}_1 \bar{m}_1 \Omega_0^2 = 0, \quad (6)$$

$$\begin{aligned} & \frac{1}{m_1} \Omega_0^2 \frac{d^2 u_n^{(1)}}{d\tau^2} - \frac{\Omega_0 \Omega_1}{\bar{m}_1} A_0 e^{ink} e^{i\tau} \\ & + \frac{1}{k_1} (2u_n^{(1)} - u_{n-1}^{(1)} - u_{n+1}^{(1)}) + (u_n^{(1)} - v_n^{(1)}) \\ & + \bar{\Gamma}_2 \left[\left(\frac{A_0}{2} e^{ink} e^{i\tau} + c \cdot c \right) - \left(\frac{B_0}{2} e^{ink} e^{i\tau} + c \cdot c \right) \right]^3 = 0, \end{aligned} \quad (7)$$

the expression of the first-order governing equation can be obtained as

$$\begin{aligned} & \frac{1}{m_1} \Omega_0^2 \frac{\partial^2 u_n^{(1)}}{\partial \tau^2} + \frac{1}{k_1} (2u_n^{(1)} - u_{n-1}^{(1)} - u_{n+1}^{(1)}) + (u_n^{(1)} - v_n^{(1)}) \\ & = c_1 e^{ink} e^{i\tau} + c_2 e^{i3nk} e^{i3\tau} + c \cdot c, \\ & c_1 = \frac{2}{m_1} \Omega_0 \Omega_1 A_0 - \frac{3}{4} \bar{\Gamma}_2 A_0^* A_0^2 (1 - \eta_w)^3. \end{aligned} \quad (8)$$

The forcing term with spatial form e^{ink} is secular and must be eliminated. Hence, $c_1 = 0$, $\Omega^{(opt)}$ and $\Omega^{(aco)}$ act as the optical mode branch and the acoustic mode branch of the structural dispersion relationship curve, and we can acquire that

$$\Omega^{(opt,aco)} = \Omega_0^{(opt,aco)} + \varepsilon \bar{\Gamma}_2 |A_0|^2 \frac{3(1 - \eta_w^{(opt,aco)})^3 \bar{m}_1}{8\Omega_0^{(opt,aco)}}. \quad (9)$$

In like manner, when $\bar{\Gamma}_1 = \frac{\Gamma_1}{k_1}$ in the EEN structure, the kinematic equations of the interior oscillator and the external matrix are

$$\begin{cases} m_1 \ddot{u}_n + k_1 (2u_n - u_{n-1} - u_{n+1}) + k_2 (u_n - v_n) \\ + \varepsilon \Gamma_1 [(u_n - u_{n-1})^3 + (u_n - u_{n+1})^3] = 0, \\ m_2 \ddot{v}_n + k_2 (v_n - u_n) = 0, \end{cases} \quad (10)$$

the dispersion relationship is established, and this situation has been calculated in Ref. 36,

$$\Omega^{(opt,aco)} = \Omega_0^{(opt,aco)} + \varepsilon \bar{\Gamma}_1 |A_0|^2 \frac{3(1 - \cos \kappa)^2}{2\Omega_0^{(opt,aco)} (\bar{k}_1 + \eta_w^{(opt,aco)} \bar{m}_1 \bar{k}_1)}. \quad (11)$$

Apart from the L-P perturbation method, the prediction method primarily hypothesizes that the structure is EIL in light of the kinematic equation of the matrix and the interior oscillator,

$$\begin{cases} m_1 \ddot{u}_n + k_1 (2u_n - u_{n-1} - u_{n+1}) + k_2 (u_n - v_n) = 0, \\ m_2 \ddot{v}_n + k_2 (v_n - u_n) = 0, \end{cases} \quad (12)$$

the EIL-LRAM's dispersion relationship can be gained,

$$\cos(\kappa) = 1 - \frac{(k_2/k_1)(\omega/\omega_0)^2 [(\omega/\omega_0)^2 - (1 + (m_2/m_1))]}{2(m_2/m_1)[(\omega/\omega_0)^2 - 1]}. \quad (13)$$

On this basis, the cubic nonlinear characteristics act as additions to a certain spring structure $k_i^{nl} = k_i + \varepsilon \Gamma_i A^2$ ($i = 1, 2$). Afterward, the constant k_i in Eq. (13) can be replaced with it. Consequently, the dispersion relationship curve related to the EEN and IEN structure can be acquired. When $A < 10^{-2} \sqrt{k_i^{nl}/|\varepsilon \Gamma_i|}$, the impact of small amplitude on k_i^{nl} can be negligible, and the structure can be regarded as a linear structure. When $A \geq 10^{-2} \sqrt{k_i^{nl}/|\varepsilon \Gamma_i|}$, $\varepsilon \Gamma_i A^2$ affects k_i^{nl} observably. Based on that, when $\varepsilon \Gamma < 0$, k_i^{nl} decreases with an increase in amplitude, and when $\varepsilon \Gamma > 0$, k_i^{nl} increases with an increase in amplitude. Summarizing from Eq. (13), the obtained structural dispersion relationship is influenced by k_1, k_2 . The softening nonlinearity and the hardening nonlinearity are expressed by the characteristics of the softening spring and the hardening spring. Two different situations with the softening spring can be considered: cubic softening spring $F_{NLS}(u) = ku - \varepsilon \Gamma u^3$,

$$\text{bilinear softening spring } F_{NLS}(u) = \begin{cases} ku - \varepsilon \Gamma u^3, & \frac{du}{du} \geq 0, \\ \frac{2k^{\frac{3}{2}} \operatorname{sgn}(u)}{3\sqrt{3}|\varepsilon \Gamma|^{\frac{1}{2}}}, & \frac{dF_{NLS}}{du} < 0. \end{cases}$$

The latter, compared with the former one, can avoid instability generated by negative stiffness and can suit the current situation. In the following research, the mentioned softening spring refers to a bilinear softening spring.

B. Characteristics of bandgap

Based on Eqs. (9), (11), and (13), the dispersion characteristics can be modulated by regulating the structural parameters. A case study of m_1 , k_1 , and k_2 is conducted to calculate the frequency dispersion relationship including both the acoustic mode and the optical mode under different parameters through the L-P perturbation method and the prediction method. Particularly, the upper bandgap is the lowest frequency in the optical mode, while the lower bandgap is the highest frequency in the acoustic mode. The frequency bandgap, also called the forbidden band, is defined as the extent between the upper bandgap and the lower bandgap, which is identified in Fig. 3(a) under the circumstance of $A = 1 \times 10^{-4}$ m.

As shown in Figs. 2(a)–2(c), the variation of internal structure parameters k_1 , m_1 , and $\varepsilon\Gamma_2$ should all be able to alter the composition of the optical mode and the acoustic mode. Moreover, k_1 increases without affecting the value of the upper bandgap, while the lower bandgap starts to shift to high frequency. Nevertheless, this phenomenon reverses when m_1 is stimulated. As a result, the location of the upper bandgap will shift to a low-frequency direction with an increase in m_1 , while the lower bandgap stays impervious. When $\varepsilon\Gamma_2 = 0$, the EEN structure is activated, when $\varepsilon\Gamma_2 = 2 \times 10^6$, k_2 shows hardening nonlinearity and the upper bandgap, and the lower bandgap moves to the high-frequency direction, and when $\varepsilon\Gamma_2 = -2 \times 10^6$, k_2 shows softening nonlinearity and the upper bandgap, and the lower bandgap moves to the low-frequency direction. The maximum errors between the prediction method and the perturbation method are 6.4%, 5.7%, and 2.6% separately. The frequency dispersion curves and the bandgap shift properties of the two individual methods are relatively identical in the same condition so the prediction method acts as an eligible succedaneum for the L-P perturbation method.

In addition, when using the perturbation method, the validity of the first-order solution can only be assured when second-order and higher-order solutions are ignorable when compared with the zero-order and first-order solutions. In this case, a series of conditions need to be satisfied. The solving process is more complicated, and the instability introduced by the softening spring's negative stiffness is non-negligible. As a result, the shift in the bandgap can be predicted, avoiding the restriction of the fact that ε is a small parameter through the prediction method. Considering the practical scale range of our research, the prediction method is selected for the latter calculation.

To assure the comparability of the impacts of k_1 and k_2 softening nonlinearities on the frequency dispersion characteristics, $\bar{\Gamma}_1 = \bar{\Gamma}_2 = 1000$ while keeping the factors in the linear structure unchanged. A battery of excitation amplitudes is chosen as $A = 1.000 \times 10^{-4}$, 0.010, 0.020, 0.050, and 0.100 m.

As shown in Fig. 3(a), in the EEN structure, with an increase in excitation amplitude A , the acoustic mode will be influenced, and the lower bandgap will shift to the low-frequency part with a small shift range. The bigger the wave vector, the optical mode will perform a more remarkable variation. However, the location of the upper bandgap remains the same while the overall frequency bandgap extends to the low-frequency part. As shown in Fig. 3(b), when IEN is activated, with an increase in excitation amplitude A , the acoustic mode will shift to the low-frequency direction and the

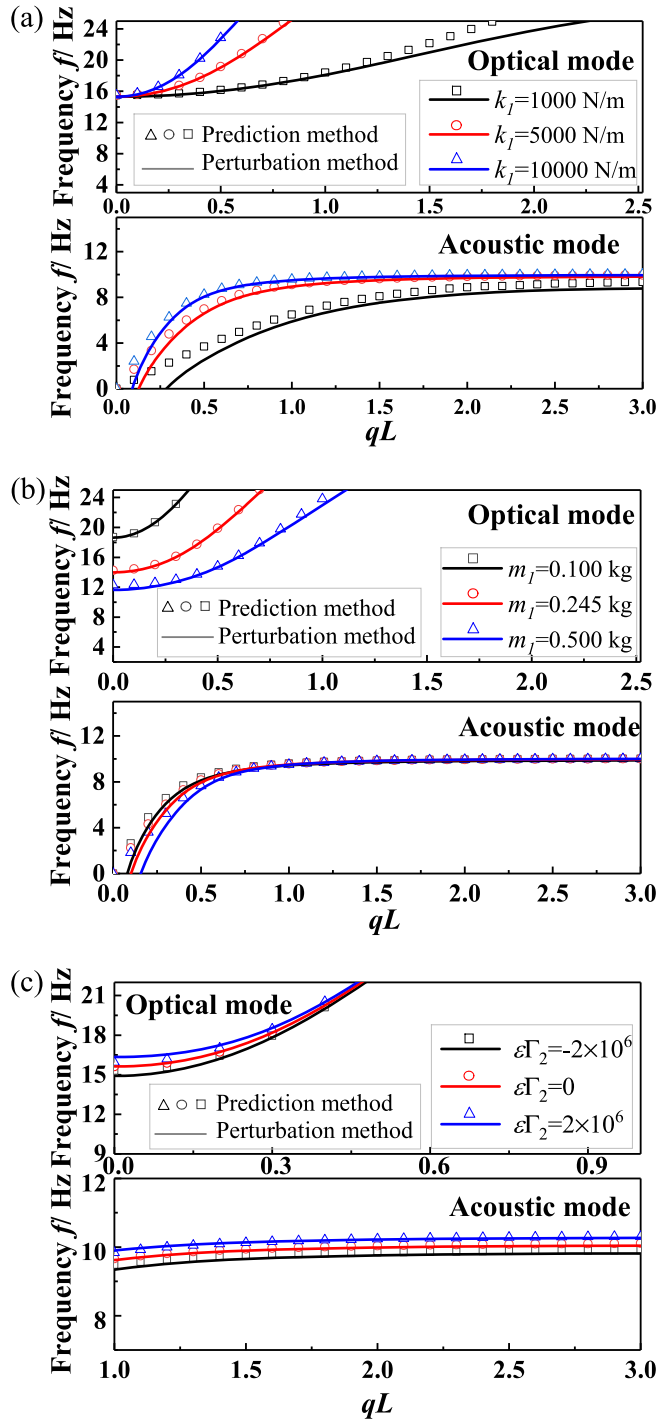


FIG. 2. The influence of parameters on softening LRAM dispersion relations calculated by the L-P perturbation method (line) and the prediction method (dot) and schematic of LRAM. (a) k_1 , when $A = 0.003$ m, $k_2 = 1000$ N/m, $m_1 = 0.180$ kg, $m_2 = 0.245$ kg, and $\varepsilon\Gamma_2 = 2 \times 10^{-6}$ in the EEN structure. (b) m_1 , when $A = 0.003$ m, $k_2 = 1000$ N/m, $k_1 = 10000$ N/m, $m_2 = 0.245$ kg, and $\varepsilon\Gamma_2 = 2 \times 10^{-6}$ in the IEN structure. (c) k_2 , when $A = 0.009$ m, $k_1 = 10000$ N/m, $m_1 = 0.180$ kg, and $m_2 = 0.245$ kg.

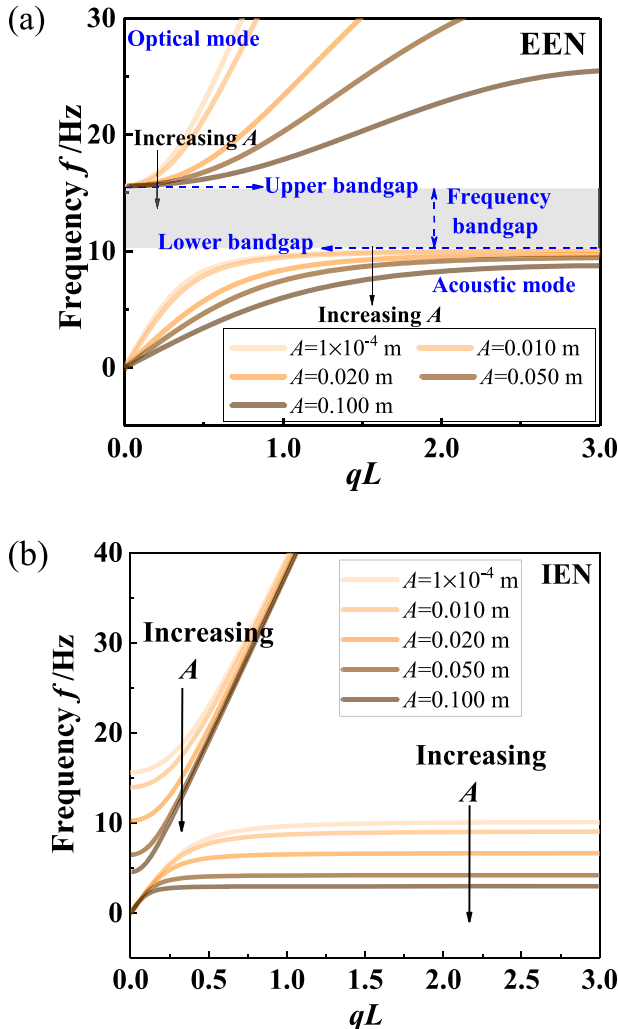


FIG. 3. The influence of excitation amplitude A on the dispersion relationship of the two softening LRAMs were calculated by the prediction method when $m_1 = 0.180 \text{ kg}$ and $m_2 = 0.245 \text{ kg}$. (a) EEN ($k_1 = 10\,000\text{--}20\,000\,000 \text{ A}^2 \text{ N/m}$ and $k_2 = 1000 \text{ N/m}$). (b) IEN ($k_2 = 1000\text{--}2000\,000 \text{ A}^2 \text{ N/m}$ and $k_1 = 10\,000 \text{ N/m}$).

corresponding lower bandgap shares the same tendency. The optical mode is affected more seriously by a small wave vector. The upper bandgap is gradually shifting to the low-frequency part. When the amplitude A is small enough, the generated bandgap equals the bandgap from EIL-LRAM, which verifies the analysis in Eq. (13).

III. RESULTS AND DISCUSSIONS OF NUMERICAL SIMULATIONS

To verify the results above through the finite-element simulation software Abaqus, a unidimensional nonlinear mass-in-mass model with the composition of 50 units is set up as shown in Fig. 1. $N_{th} \geq 16$ units add exponentially increasing damping $c = (N_{th} - 15)^2 \times 0.1 \text{ N/(m/s)}$ as vibration absorbers to avoid disturbance from reflected signals. According to three different

structures, such as EIL, EEN, and IEN, individual factors are designated,

$$[m_1, m_2, k_1, k_2, \varepsilon\Gamma_1, \varepsilon\Gamma_2, L] = [0.180 \text{ kg}, 0.245 \text{ kg}, 1 \times 10^4 \text{ N/m}, 1 \times 10^3 \text{ N/m}, 0, 0, 1 \text{ m}],$$

$$[m_1, m_2, k_1, k_2, \varepsilon\Gamma_1, \varepsilon\Gamma_2, L] = [0.180 \text{ kg}, 0.245 \text{ kg}, 1 \times 10^4 \text{ N/m}, 1 \times 10^3 \text{ N/m}, -2 \times 10^7, 0, 1 \text{ m}],$$

$$[m_1, m_2, k_1, k_2, \varepsilon\Gamma_1, \varepsilon\Gamma_2, L] = [0.180 \text{ kg}, 0.245 \text{ kg}, 1 \times 10^4 \text{ N/m}, 1 \times 10^3 \text{ N/m}, 0, -2 \times 10^7, 1 \text{ m}].$$

To validate the feasibility of designing the following ATC, in the following simulation, concentrated force CF is utilized to represent the excitation amplitude A in the simulation. When the driving frequency reaches f_0 , A_1 and A_{15} , the input and output time-domain signals from $N_{th} = 1$ and 15, transform into frequency-domain signals $F(A_1)$ and $F(A_{15})$ through FFT. The amplitudes of frequency-domain signals that fall at frequency f_0 are $F_{f_0}(A_1)$ and $F_{f_0}(A_{15})$. The transmission factor under this frequency is $T_{f_0} = F_{f_0}(A_{15})/F_{f_0}(A_1)$. Frequency sweep computing is conducted with an interval frequency of 0.2 Hz to obtain the transmission factor curve of EIL, EEN, and IEN under different orders of magnitude of driving input.

As shown in Fig. 4(a), in the EIL-LRAM, considering diverse amplitude input T remains unchanged because of the lack of nonlinearity. The frequency zone where transmission factor $T < 0.2$ is 10.05–15.58 Hz, which is almost identical on equal terms with the theoretical calculation and thus results in using T to stand for the bandgap location. When the driving frequency is low enough, the situation $T > 1$ appears. This is generated by the mismatch of the wavelength and the size of the structure. In Fig. 4(b), the structure is EEN-LRAM, $CF = 8, 400$, and 1000, and the homologous band gaps are 10.14–15.88, 7.90–15.88, and 5.90–15.57 Hz, respectively. The structure is IEN-LRAM as shown in Fig. 4(c), and the bandgaps are 10.12–15.83, 4.90–7.80, and 3.25–4.92 Hz along with an increase in CF . With small amplitude input $CF = 8 \text{ N}$, the nonlinear term is impervious, and the bandgap introduced by EEN and IEN has in common with the one from EIL. All the results verify the bandgap migration rule obtained from the theoretical calculation.

This work, respectively, investigates the impact of the excitation amplitude on the propagation properties of EEN and IEN when single-frequency f and dual-frequency f_1 and f_2 excitation. Entire results shown in Figs. 5(a) and 3(b) conform to the transmission factors under corresponding conditions in Figs. 4(b) and 3(c).

Worthy of note is that when a single frequency operates, $CF = 400 \text{ N}$ in EEN, the attenuation rate of the amplitude is 38.9% and only increases to 79.2% even though $CF = 1000 \text{ N}$. However, the attenuation rate is 93.9%, which shows greater amplitude attenuation as early as $CF = 400 \text{ N}$ in IEN. According to $CF = 1000 \text{ N}$, the IEN structure can shift from attenuated to non-attenuated slick. When the driving input has two frequencies (f_1 and f_2), there exist

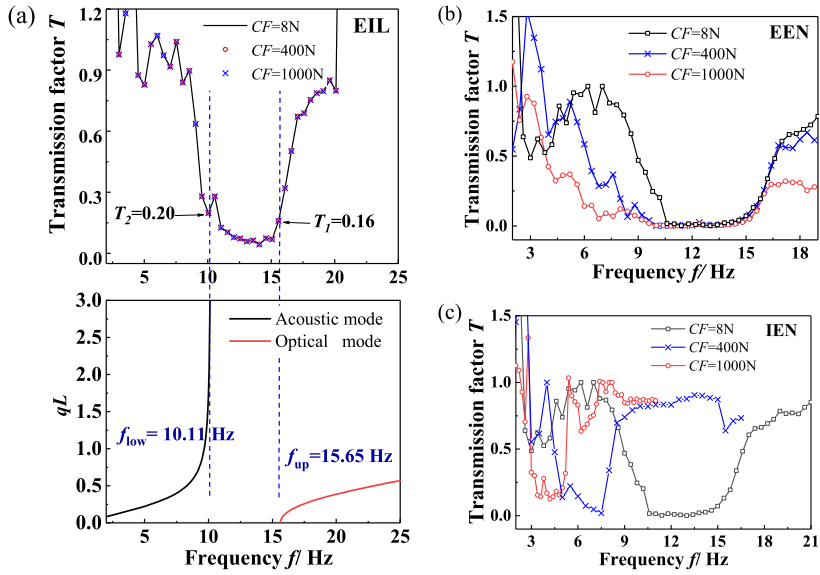


FIG. 4. Transmission factors obtained by simulation when the input stress $CF = 8\text{ N}$ (black), $CF = 400\text{ N}$ (blue), and $CF = 1000\text{ N}$ (red). (a) EIL (up) and its theoretical dispersion curve (down). (b) EEN. (c) IEN.

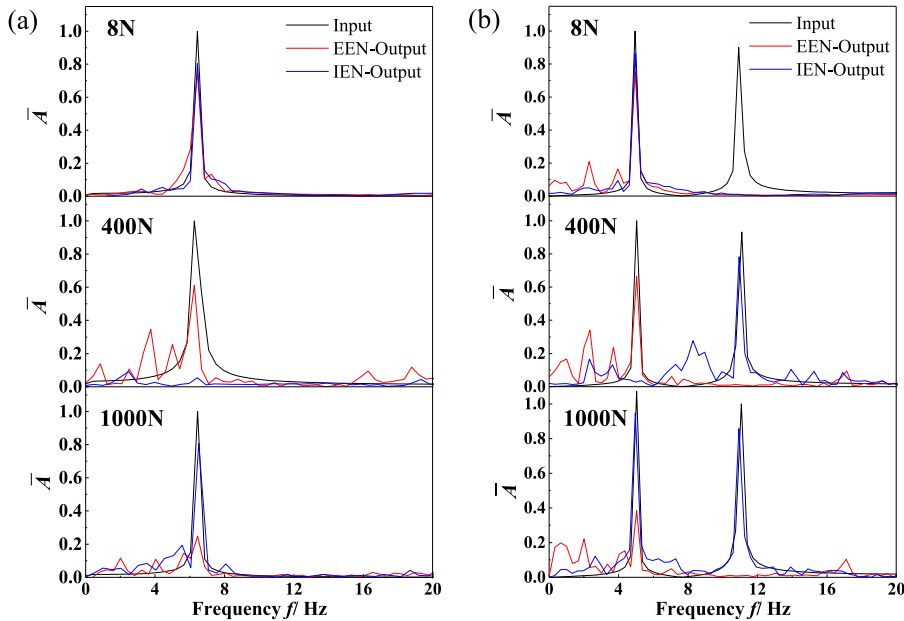


FIG. 5. Received frequency domain signals of normalized amplitude \bar{A} at $N_{th} = 1$ (black) and $N_{th} = 15$ (red or blue) when input single or dual frequency signal with variant stresses. (a) $f_0 = 6.5\text{ Hz}$. (b) $f_1 = 5\text{ Hz}$ and $f_2 = 11\text{ Hz}$.

four demands $(1, 0)$, $(0, 1)$, $(0, 0)$, and $(1, 1)$, where 0 and 1 represent attenuation and pass, respectively. In the EEN structure, it appears to be $(1, 0)$ in the frequency domain for diverse CF . Additionally, the structure of IEN shows $(1, 0)$, $(0, 1)$, and $(1, 1)$. In the multi-functional SMs, selectively conducting attenuation and signal reservation of certain frequencies based on different vibration types is essential, and an obvious frequency shift phenomenon in the dominant frequency signal is forbidden. As a result, the IEN structure suits the research of multi-functional SMs better.

IV. ACOUSTIC THREE-TERMINAL CONTROLLER

A. Research of quantitative relationship

In the following research, the quantitative relationship between upper bandgap, lower bandgap, width, and the excitation is studied. The relationship between concentrated force CF and amplitude A is shown in Table I. Taking advantage of the finite-element simulation method, the research acquires the bandgap location and the width represented by the transmission factor in Table I, as shown in Fig. 6,

TABLE I. The relationship between the input concentration force CF and the input displacement A in the simulation.

CF/N	A/m	CF/N	A/m
8	6×10^{-4}	400	0.048
50	0.003	600	0.057
100	0.007	800	0.081
200	0.019	1000	0.099
300	0.031

with the concentrated force as the external excitation. Among the rest, the point diagram stands for the simulation result, while the line graph acts as the presentation of the prediction method.

As concluded from Fig. 6(a), in the EEN structure, the upper bandgap is immune to the variation of amplitude, and the lower bandgap is inversely proportional to the amplitude. The corresponding bandgap width is directly proportional to the amplitude. Comparing the simulation result and the theoretical result, despite the deviation under large amplitude, the overall trends are

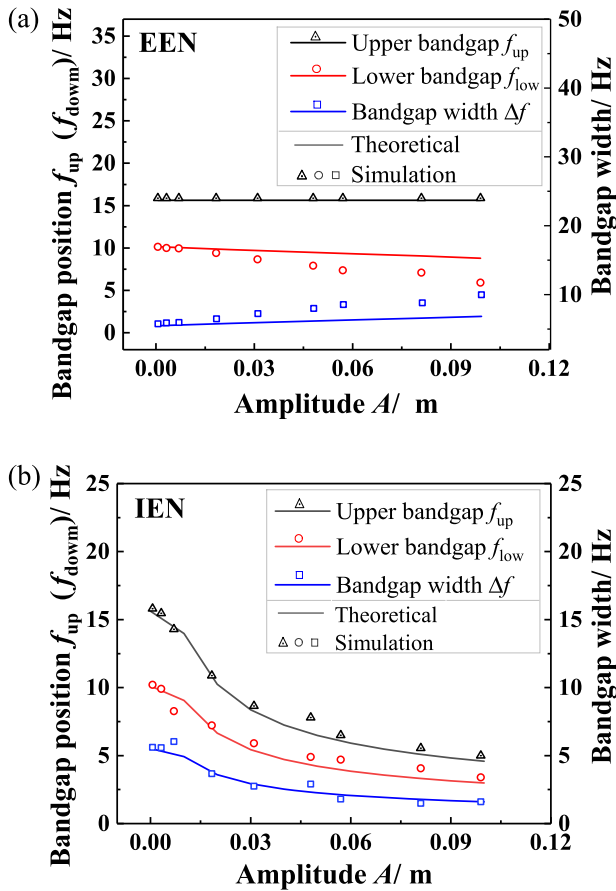


FIG. 6. Relationships between the upper bandgap (black), lower bandgap (red), width (blue) of the bandgap, and the concentrating force obtained by theoretical calculation (line) and simulation (point). (a) EEN. (b) IEN.

identical. As shown in Fig. 6(b), in the IEN structure, the upper bandgap, the lower bandgap, and the bandgap width are inversely proportional to the amplitude, in both simulation and theoretical results. When $A < 0.020$ m, the bandgap shows exponentially shifting to the low-frequency part. When $A > 0.020$ m, the migration velocity approaches a flat. At the same time, the bandgap width decreases gradually, and the decreasing speed matches the tendency of the changing bandgap migration velocity. The amplitude shares a fitting quantitative relationship with the upper bandgap, the lower bandgap, and the bandgap width of the nonlinear mass-in-mass system. The average error of the simulation and theoretical results is 7.2%.

B. ATC model

Based on the above analysis, an ATC is proposed in this section, as shown in Fig. 7. It consists of an input port, a control port, and an output port. In addition, the IEN-LRAM structure and the input port can be assumed to be immutable regions. This acoustical device is predicted to be able to modulate the bandgap location of the IEN-LRAM structure and the signal from the output port without changing the input signal and the device parameters. The original bandgap of IEN-LRAM is $[f_1, f_2]$, and the input signal's frequency is f_0 with the amplitude of A_0 . On the condition that $f_0 \notin [f_1, f_2]$, a control signal with a frequency of f_c and an amplitude of A_c is loaded. The bandgap $[f_1, f_2]$ shifts with the variation of A_c , and the average amplitude³⁴ of A_c and A_0 has a quantitative relationship with the bandgap offset as shown in Figs. 6(a) and 6(b). As a consequence, the shifted bandgap $[f'_1, f'_2]$ that includes the incident frequency f_0 can be ensured by adjusting the amplitude of A_c to guarantee the attenuation of the input signal. Apart from that, $f_c \in [f'_1, f'_2]$ is supposed to render certain, which ensures that the signal from the control port attenuates totally in the structure so as not to disturb the receipt signal.

C. Verification of function implementation

In the simulation, the designed ATC based on Sec. III' IEN-model parameters has an operating frequency range of below 16.00 Hz because of the bandgap migration generated by the variation in excitation amplitude. The input port where $N_{th} = 1$ is loaded with the input signals $f_0 = 7.00$ Hz and $A_0 = 7.5 \times 10^{-4}$ m (which equal the displacement of the structure when $CF = 20$ N). The location where $N_{th} = 25$ is the output port. The time-domain and the frequency-domain signals from the input port are shown in Fig. 8(a). When $F_c = 150$ N and the frequency of the control port $f_c = 10.00$ Hz, the result is depicted in Fig. 8(b). When $F_c = 150$ N and $F_c = 0$ N, the output port's result is depicted in Fig. 8(c).

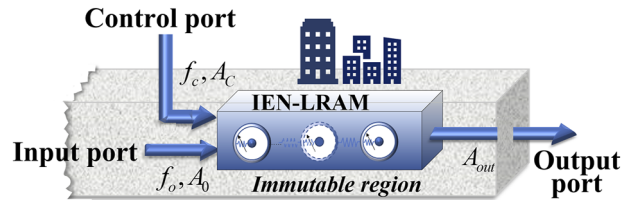


FIG. 7. Schematic diagram of an ATC.

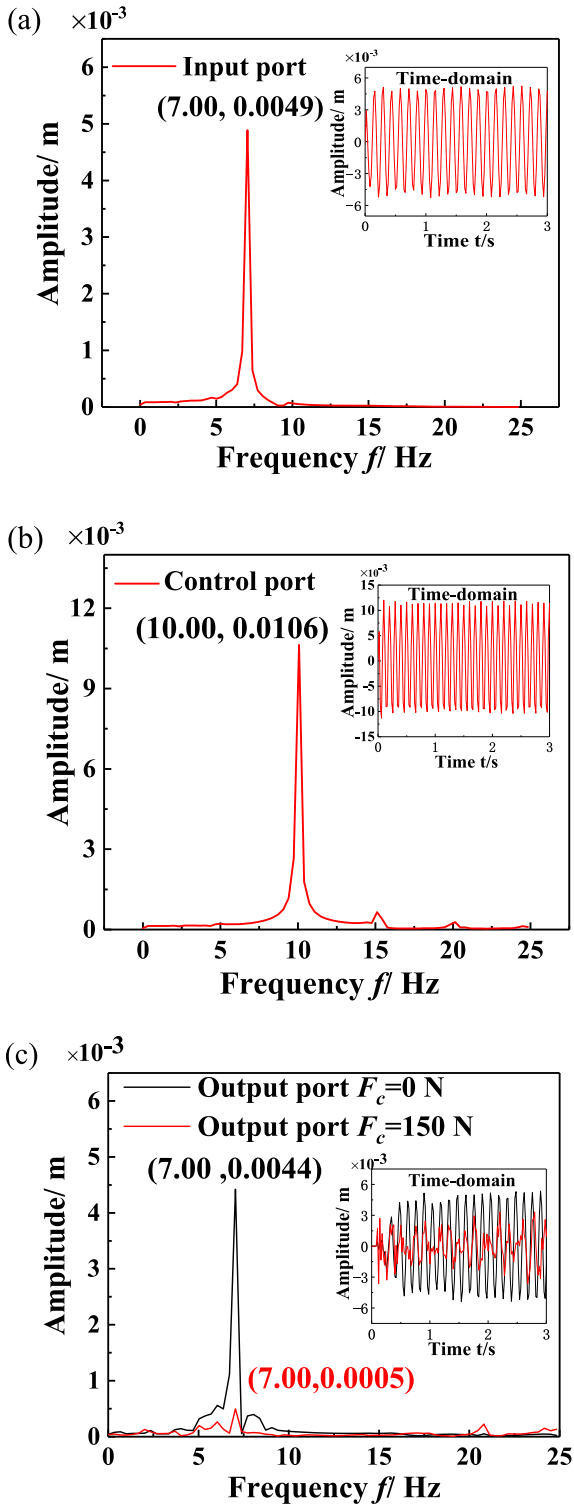


FIG. 8. Three-terminal signals. (a) Input signals in the time domain and the frequency domain. (b) Time domain and frequency domain signal input by the control port when $F_c = 150$ N. (c) Time domain and frequency domain signals at the output port when $F_c = 0$ N and $F_c = 150$ N.

When $F_c = 0$ N, the bandgap is 10.05–15.58 Hz, and the incident frequency locates in the passband. Concluded from Fig. 8(a) and the black line in Fig. 8(c), the input signal shows almost no signs of attenuation. When $F_c = 150$ N, the bandgap migrates to 6.89–10.41 Hz, and the incident frequency belongs to the bandgap. Comparing Fig. 8(a) and the red lines in Fig. 8(c), the amplitude at the receiving end attenuates massively. The attenuation rate of the amplitude $\alpha = 1 - A_{out}/A_0$. The 7 Hz sound wave signal is determined by the control terminal according to Fig. 8(c). The attenuation rate is 9.6% when the control port is unloaded and it increases to 90.2% with a loaded control port. Analyzing Fig. 8(b) and the red lines in Fig. 8(c), an appropriate input with the frequency of f_c at the control port brings favorable attenuation of 99.1% in the bandgap to avoid influencing the frequency component at the receiving port. The relationship between the input stress F_c at the control port and the attenuation rate α of the output port signal is obtained.

As shown in Fig. 9, the changing of F_c will exert different impacts on the output signal propagating through ATC. When $F_c = 0$ N, $\alpha = 9.6\%$, the signal from the input port can smoothly pass through the structure. When $F_c \in (0, 150)$ N, $\alpha < 90.0\%$. In the red dotted box, $F_c \in [150, 300]$ N and $\alpha > 90.0\%$. In this region, specific F_c can be chosen to fulfill the attenuation of the 7.00 Hz input signal because of the 20 dB reduction in sound pressure. When $F_c = 190$ N, $\alpha_{max} = 98.7\%$, and the damping effect is the best. When $F_c > 400$ N, α appears to fluctuate irregularly but amplitude remains above 80.0%. In analysis, the existence of a nonlinear structure introduces frequency migration. On the other hand, with an increase in the amplitude, the bandgap's migration velocity decreases gradually, and the transmission factor shows mild variation. However, this does not affect the selection of the external stress to reach the best amplitude attenuation rate. The mass-in-mass model of SM in this paper is a kind of LRAMs. Therefore, other types of LRAMs can be used practically in SMs, and the nonlinear parameters can be introduced in other ways instead of being limited to the form of springs.^{20,38,40} With this research, we are expected to achieve three goals: to attenuate seismic waves like conventional SMs; to shift the

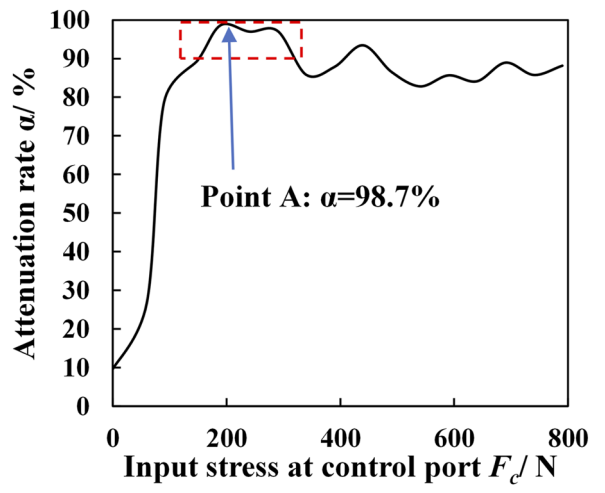


FIG. 9. Diagram of the relationship between the input stress of the control port and the signal attenuation rate of the output port.

bandgap to burst low-frequency vibration band area; and to gather and utilize seismic wave energy of a specific frequency band. Prevention and control of different types of low-frequency vibration are supposed to be realized with pertinence and high efficiency and can be expanded to multi-functional SMs.

V. CONCLUSION

In this paper, based on the amplitude-dependence periodic chain structure frequency bandgap with nonlinear effect, a comparative study is conducted between three individual structure models of LRAMs: EIL, EEN, and IEN. The dispersion curves are obtained with the prediction method and the L-P perturbation method, and the impact of the external excitation amplitude on the forbidden bands of the EEN and IEN structures is calculated. The work also investigates the transmission factor and the dynamic response when single-frequency and dual-frequency waves propagate through three structures under different stimulations and incident frequencies. It is validated that the upper bandgap is immune to the variation of the amplitude, and the lower bandgap will shift to the low-frequency direction with the increasing of excitation amplitude in the EEN structure. In the IEN structure, the bandgap is supposed to migrate toward the low-frequency part, and there is a quantitative relationship between the migration and the amplitude. Additionally, the concept of ATC is proposed, and a preliminary validity simulation is performed. The function of modulating the input signal through external controlling of the acoustic device without changing the device's structure is achieved. The proposal of ATC can not only broaden the category of subsize acoustic devices but also provide a resultful scheme for the designing of external-controllable multi-functional SMs.

ACKNOWLEDGMENTS

This work was supported by the National Key R & D Program of China (Grant No. 2020YFA0211400), the State Key Program of the National Natural Science of China (Grant No. 11834008), the National Natural Science Foundation of China (Grant Nos. 12174192 and 11774167), the State Key Laboratory of Acoustics, Chinese Academy of Science (Grant No. SKLA202210), and the Key Laboratory of Underwater Acoustic Environment, Chinese Academy of Sciences (Grant No. SSHJ-KFKT-1701).

AUTHOR DECLARATIONS

Conflict of Interest

The authors have no conflicts to disclose.

Author Contributions

Yuanyuan Li: Data curation (lead); Formal analysis (equal); Investigation (equal); Writing – original draft (lead). **Jiancheng Liu:** Data curation (equal); Formal analysis (equal); Investigation (equal). **Zhaoyu Deng:** Data curation (equal); Formal analysis (equal); Investigation (equal). **Menyang Gong:** Data curation (equal); Formal analysis (equal); Investigation (equal). **Kunqi Huang:** Data curation (equal); Formal analysis (equal); Methodology (equal). **Yun Lai:** Investigation (equal); Supervision (equal); Writing – original draft

(equal); Writing – review & editing (equal). **Xiaozhou Liu:** Conceptualization (lead); Funding acquisition (lead); Investigation (equal); Project administration (lead); Supervision (lead); Writing – original draft (equal); Writing – review & editing (equal).

DATA AVAILABILITY

The data that support the findings of this study are available from the corresponding author upon reasonable request.

REFERENCES

- ¹H. H. Huang and C. T. Sun, *J. Mech. Phys. Solids* **59**, 2070 (2011).
- ²B. Emanuele, M. Carrara, and M. Ruzzene, *Health Monitoring of Structural and Biological Systems* (SPIE, CA, 2003), p. 86925.
- ³P. Sheng, X. X. Zhang, Z. Liu, and C. T. Chan, *Physica B* **338**, 201 (2003).
- ⁴A. L. Chen, Q. Y. Tang, H. Y. Wang, S. D. Zhao, and Y. S. Wang, *Sci. China Phys. Mech.* **63**, 244611 (2020).
- ⁵W. J. Zhou, B. Wu, Muhammad, Q. J. Du, G. L. Huang, C. F. Lü, and W. Q. Chen, *J. Appl. Phys.* **123**, 165304 (2018).
- ⁶H. H. Huang, C. T. Sun, and G. L. Huang, *Int. J. Eng. Sci.* **47**, 610 (2009).
- ⁷Z. Zhu, Y. Yang, N. Z. Zhang, L. Liu, C. S. Sheng, M. M. Jia, and C. Shan, *Science* **289**, 1734 (2000).
- ⁸H. Zheng, C. Z. Zhang, Y. S. Wang, J. Sladek, and V. Sladek, *Eng. Anal. Boundary Elem.* **66**, 77 (2016).
- ⁹P. Yan, J. O. Vasseur, B. Djafari-Rouhani, L. Dobrzański, and P. A. Deymier, *Surf. Sci. Rep.* **65**, 229 (2010).
- ¹⁰F. Casadei, T. Delpero, A. Bergamini, P. Ermanni, and M. Ruzzene, *J. Appl. Phys.* **112**, 141 (2012).
- ¹¹K. H. Matlack, A. Bauhofer, S. Krödel, A. Palermo, and C. Daraio, *Proc. Natl. Acad. Sci. U.S.A.* **113**, 8386 (2016).
- ¹²P. Sheng and M. Yang, *Annu. Rev. Mater. Res.* **41**, 83 (2017).
- ¹³J. Li, Y. Yuan, J. Wang, R. H. Bao, and W. Q. Chen, *Int. J. Impact Eng.* **156**, 103924 (2021).
- ¹⁴J. M. Manimala and C. T. Sun, *J. Appl. Phys.* **115**, 557 (2014).
- ¹⁵M. Hirsekorn, *Appl. Phys. Lett.* **84**, 3364 (2004).
- ¹⁶S. Zhang, J. Hua, and J. C. Cheng, *Chin. Phys. Lett.* **20**, 1303 (2003).
- ¹⁷M. Hirsekorn, P. P. Delsanto, N. K. Batra, and P. Matic, *Ultrasonics* **42**, 231 (2004).
- ¹⁸W. J. Zhou, Muhammad, W. Q. Chen, Z. Y. Chen, and C. W. Lim, *Eur. J. Mech. A* **77**, 103807 (2019).
- ¹⁹Y. Xiao, J. H. Wen, and X. S. Wen, *J. Phys. D: Appl. Phys.* **45**, 195401 (2012).
- ²⁰G. Finocchio, O. Casablanca, G. Ricciardi, U. Alibrandi, F. Garesci, M. Chiappini, and B. Azzerboni, *Appl. Phys. Lett.* **104**, 509 (2014).
- ²¹S. Krödel, N. Thomé, and C. Daraio, *Extreme Mech. Lett.* **4**, 111 (2015).
- ²²D. J. Colquitt, A. Colombi, R. V. Craster, P. Roux, and S. R. L. Guenneau, *J. Mech. Phys. Solids* **99**, 379 (2016).
- ²³Y. Achaoui, T. Antonakakis, S. Brûlé, R. V. Craster, S. Enoch, and S. Guenneau, *New J. Phys.* **19**, 063022 (2017).
- ²⁴P. Antonio, V. Matteo, and M. Alessandro, *Soil Dyn. Earthquake Eng.* **113**, 265 (2018).
- ²⁵B. Francesco, W. Moritz, S. B. Oreste, and F. Marinella, *Earthquake Eng. Struct. Dyn.* **48**, 232 (2018).
- ²⁶A. Colombi, P. Roux, S. Guenneau, P. Gueguen, and R. V. Craster, *Sci. Rep.* **6**, 19238 (2016).
- ²⁷Y. F. Liu, J. K. Huang, Y. G. Li, and Z. F. Shi, *Constr. Build. Mater.* **199**, 737 (2019).
- ²⁸M. I. Hussein, M. J. Leamy, and M. Ruzzene, *Appl. Mech. Rev.* **66**, 040802 (2014).
- ²⁹M. H. Bae and J. H. Oh, *J. Mech. Phys. Solids* **139**, 103930 (2020).

- ³⁰N. Boechler, C. Daraio, R. K. Narisetti, M. Ruzzene, and M. J. Leamy, *Iutam Bookseries* (Springer Science, 2010), Vol. 26, p. 209.
- ³¹J. M. Manimala and C. T. Sun, *J. Acous. Soc. Am.* **139**, 3365 (2016).
- ³²A. F. Vakakis and M. E. King, in Presented at the Proceedings of the 1995 ASME Design Engineering Technical Conference, Boston, America, 1995.
- ³³R. K. Narisetti, M. J. Leamy, and M. Ruzzene, *J. Vib. Acoust.* **132**, 031001 (2010).
- ³⁴K. Manktelow, M. J. Leamy, and M. Ruzzene, *Nonlinear Dyn.* **63**, 193 (2011).
- ³⁵R. K. Narisetti, M. Ruzzene, and M. J. Leamy, *Wave Motion* **49**, 394 (2012).
- ³⁶W. J. Zhou, X. P. Li, Y. S. Wang, W. Q. Chen, and G. L. Huang, *J. Sound. Vib.* **413**, 250 (2018).
- ³⁷R. Zivieri, F. Garesci, B. Azzerboni, M. Chiappini, and G. Finocchio, *J. Sound. Vib.* **462**, 114929 (2019).
- ³⁸P. P. Kulkarni and J. M. Manimala, *Acta Mech.* **230**, 2521 (2019).
- ³⁹S. Fiore, G. Finocchio, R. Zivieri, M. Chiappini, and F. Garesci, *Appl. Phys. Lett.* **117**, 124101 (2020).
- ⁴⁰M. H. Bae and J. H. Oh, *Mech. Syst. Signal Process.* **170**, 108832 (2022).